Hollow helices as high-affinity hosts: Single and double helical pseudofoldaxanes

Yulong Zhong,‡[a] Thomas A. Sobiech,‡[a] Brice Kauffmann,[b] Bo Song,[c] Xiaopeng Li,[c] Yan Ferrand,[b] Ivan Huc[d] and Bing Gong*[a]

[a] Department of Chemistry University at Buffalo, The State University of New York Buffalo, New York 14260, USA. E-mail: bgong@buffalo.edu

[b] Institut de Chimie et Biologie des Membranes et des Nano-objets, UMR 5248 CNRS, Universite de Bordeaux, F33600 Pessac, France

[c] Department of Chemistry, Northwestern University Evanston, IL 60208, USA

[d] College of Chemistry and Environmental Engineering, Shenzhen University, Shenzhen, Guangdong 518060

[e] Department Pharmazie, Ludwig-MaximiliansUniversitat Munchen, D-81377 Munich, Germany

Supporting Information

I. Supporting Figures

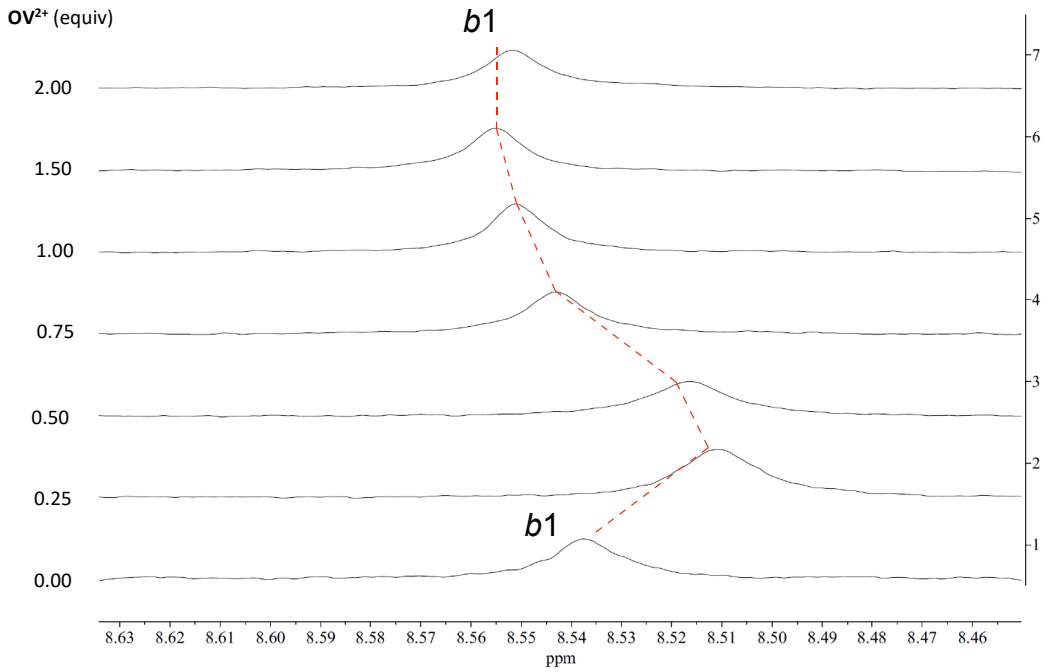

Figure S1. Partial ^{1}H NMR (500 MHz) spectra of **H8** (1 mM) titrated with 0 to 2 equiv of **OV^{2+}** in DMSO-d_6/$CDCl_3$ (3/7, v/v) at 45 °C

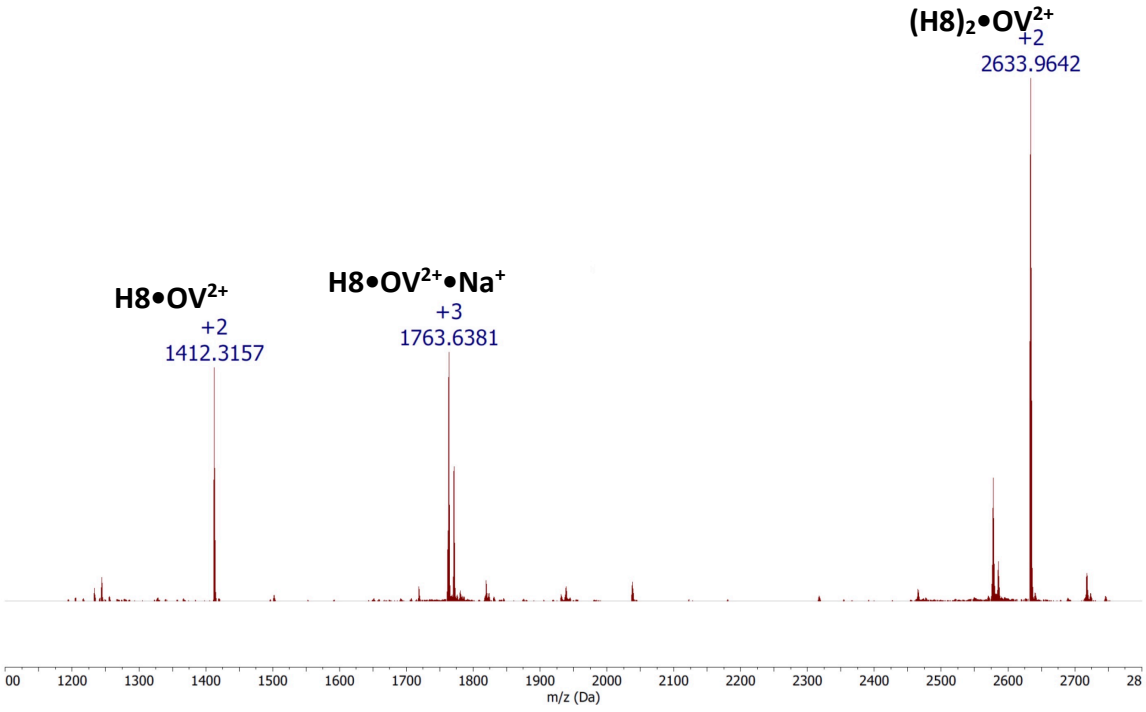

Figure S2a-1. High-resolution electrospray-ionization quadrupole time-of-flight (ESI-TOF) spectrum of the 2:1 mixture of **H8** and **OV^{2+}•$(PF_6^-)_2$.**

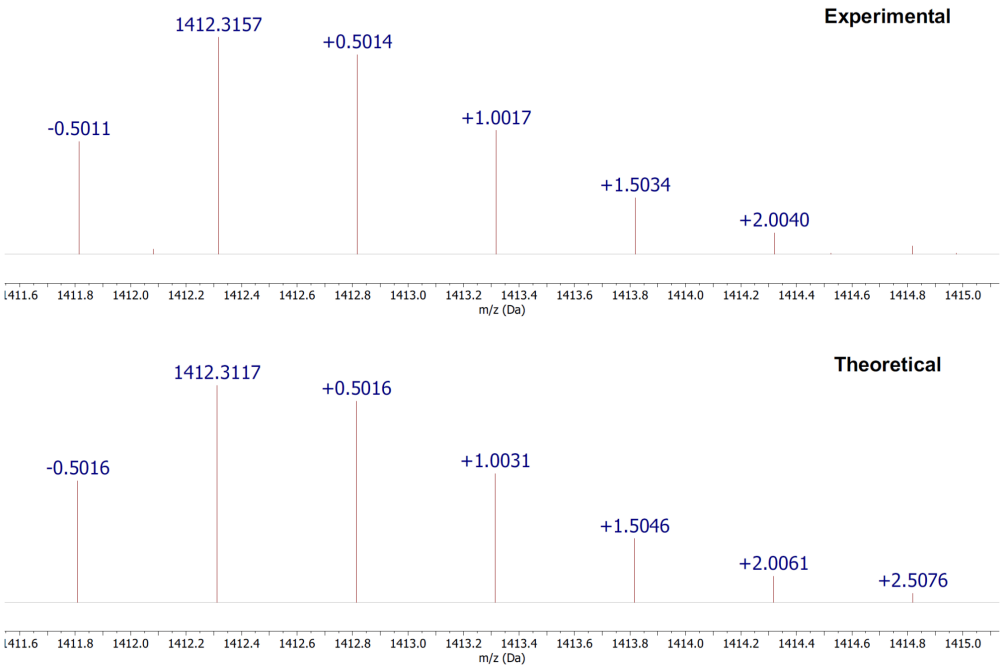

Figure S2a-2. Isotope distributions of ion **H8·OV^{2+}** in the 2:1 mixture of **H8** and **OV^{2+}•(PF_6^-)$_2$** (upper: from ESI-QTOF spectrum; bottom: from computer simulation). The mass difference between isotope peaks is about 0.5 (1/2).

Figure S2a-3. Isotope distributions of ion **(H8)$_2$·OV^{2+}•Na$^+$** in the 2:1 mixture of **H8** and **OV^{2+}•(PF_6^-)$_2$** (upper: from ESI-QTOF spectrum; bottom: from computer simulation). The mass difference between isotope peaks is about 0.33 (1/3).

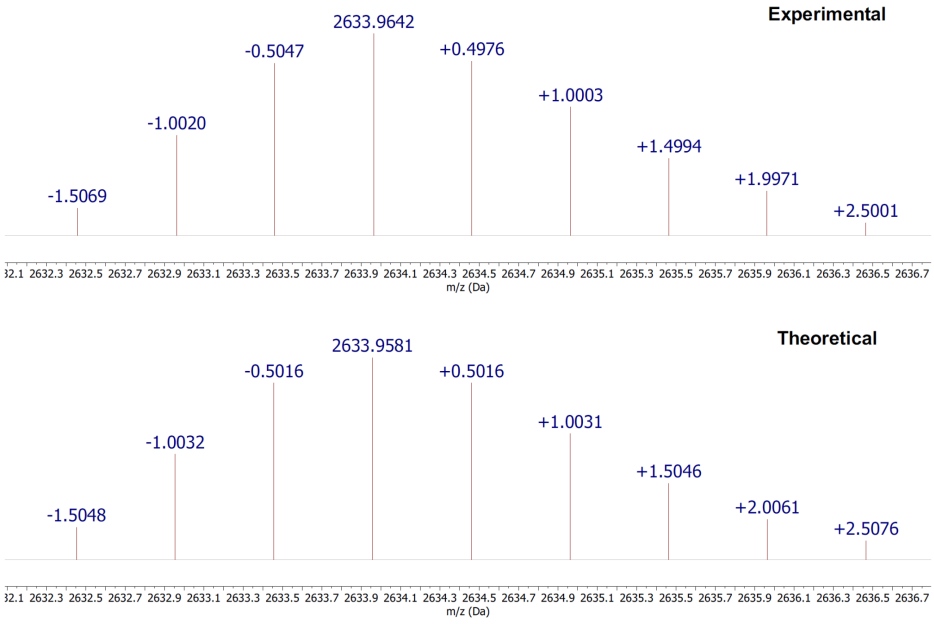

Figure S2a-4. Isotope distributions of ion $(\mathbf{H8})_2 \cdot \mathbf{OV}^{2+}$ in the 2:1 mixture of **H8** and $\mathbf{OV}^{2+} \bullet (\mathbf{PF_6}^-)_2$ (upper: from ESI-QTOF spectrum; bottom: from computer simulation). The mass difference between isotope peaks is about 0.5 (1/2).

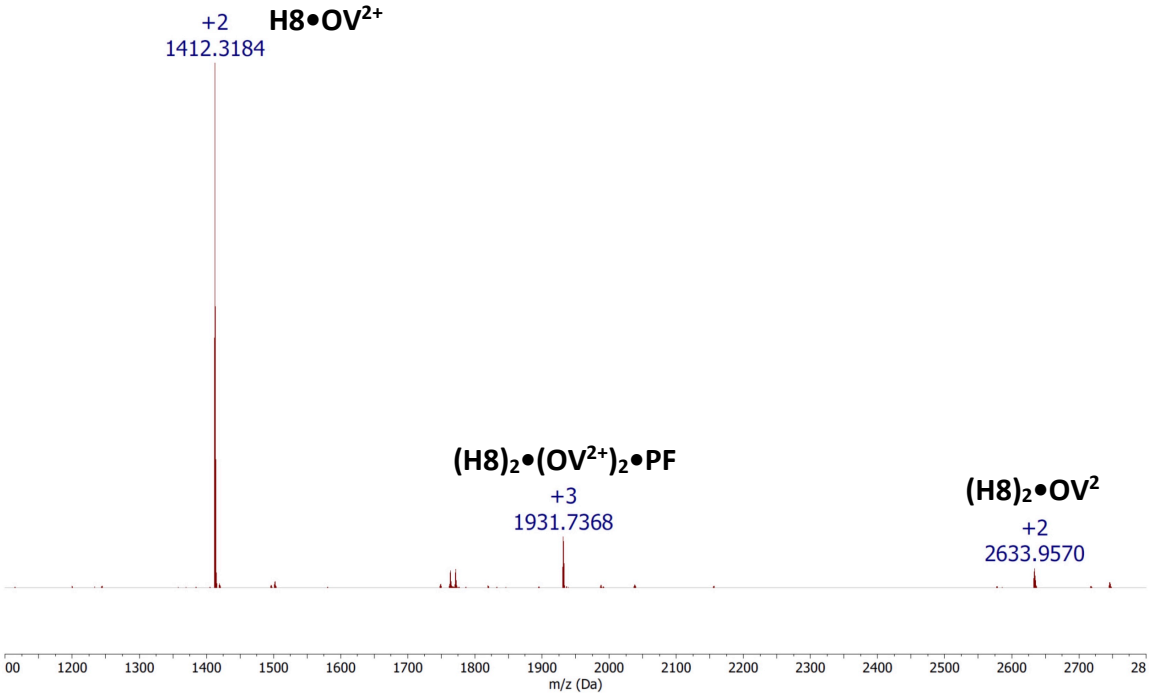

Figure S2b-1. High resolution electrospray-ionization quadrupole time-of-flight (ESI-TOF) spectrum of the 1:1 mixture of **H8** and $\mathbf{OV}^{2+} \bullet (\mathbf{PF_6}^-)_2$.

Figure S2b-2. Isotope distributions of ion **$(H8)_2 \cdot OV^{2+}$** in the 1:1 mixture of **H8** and **$OV^{2+} \bullet (PF_6^-)_2$** (upper: from ESI-QTOF spectrum; bottom: from computer simulation). The mass difference between isotope peaks is about 0.5 (1/2).

Figure S2b-3. Isotope distributions of ion **$(H8)_2 \cdot (OV^{2+})_2 \bullet PF_6^-$** in the 1:1 mixture of **H8** and **$OV^{2+} \bullet (PF_6^-)_2$** (upper: from ESI-QTOF spectrum; bottom: from computer simulation). The mass difference between isotope peaks is about 0.33 (1/3).

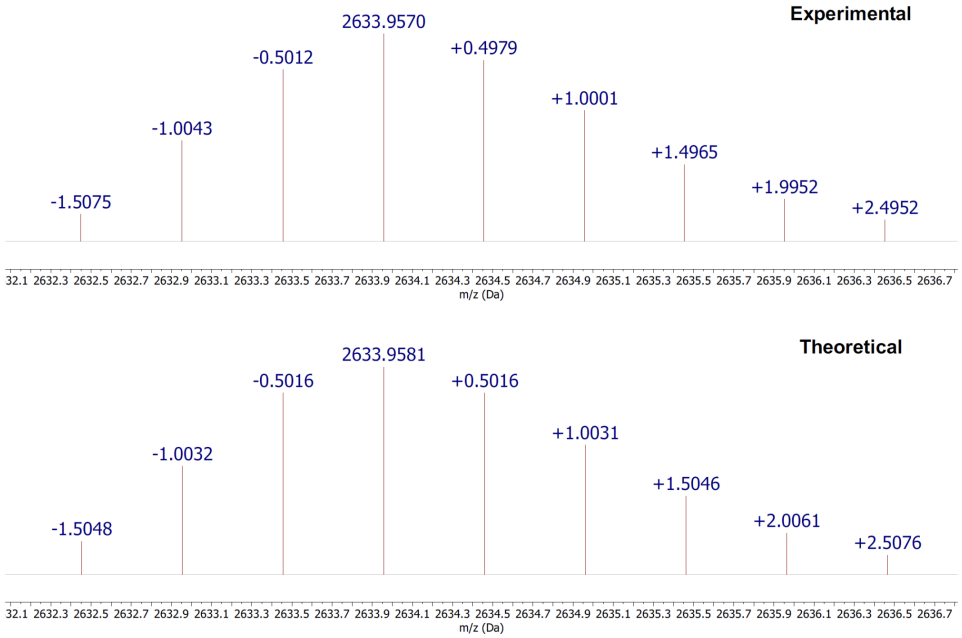

Figure S2b-4. Isotope distributions of ion $(\mathbf{H8})_2 \cdot \mathbf{OV}^{2+}$ in the 1:1 mixture of **H8** and $\mathbf{OV}^{2+} \bullet (\mathbf{PF_6}^-)_2$ (upper: from ESI-QTOF spectrum; bottom: from computer simulation). The mass difference between isotope peaks is about 0.5 (1/2).

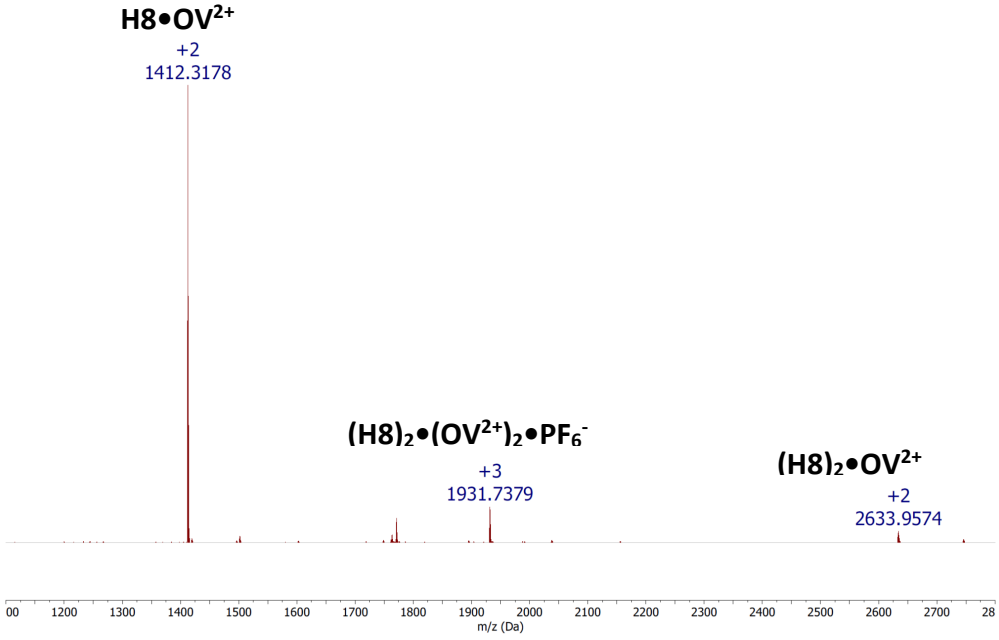

Figure S2c-1. High resolution electrospray-ionization quadrupole time-of-flight (ESI-TOF) spectra of the 1:2 mixture of **H8** and $\mathbf{OV}^{2+} \bullet (\mathbf{PF_6}^-)_2$

Figure S2c-2. Isotope distributions of ion **H8·OV^{2+}** in the 1:2 mixture of **H8** and **OV^{2+}•(PF$_6^-$)$_2$** (upper: from ESI-QTOF spectrum; bottom: from computer simulation). The mass difference between isotope peaks is about 0.5 (1/2).

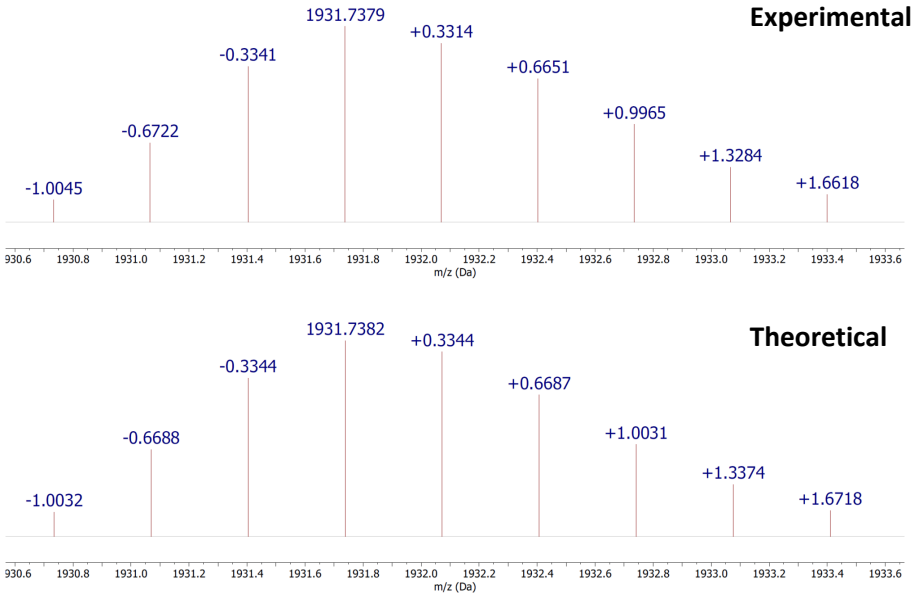

Figure S2c-3. Isotope distributions of ion **(H8)$_2$·(OV^{2+})$_2$•**PF$_6^-$ in the 1:2 mixture of **H8** and **OV^{2+}•(PF$_6^-$)$_2$** (upper: from ESI-QTOF spectrum; bottom: from computer simulation). The mass difference between isotope peaks is about 0.33 (1/3).

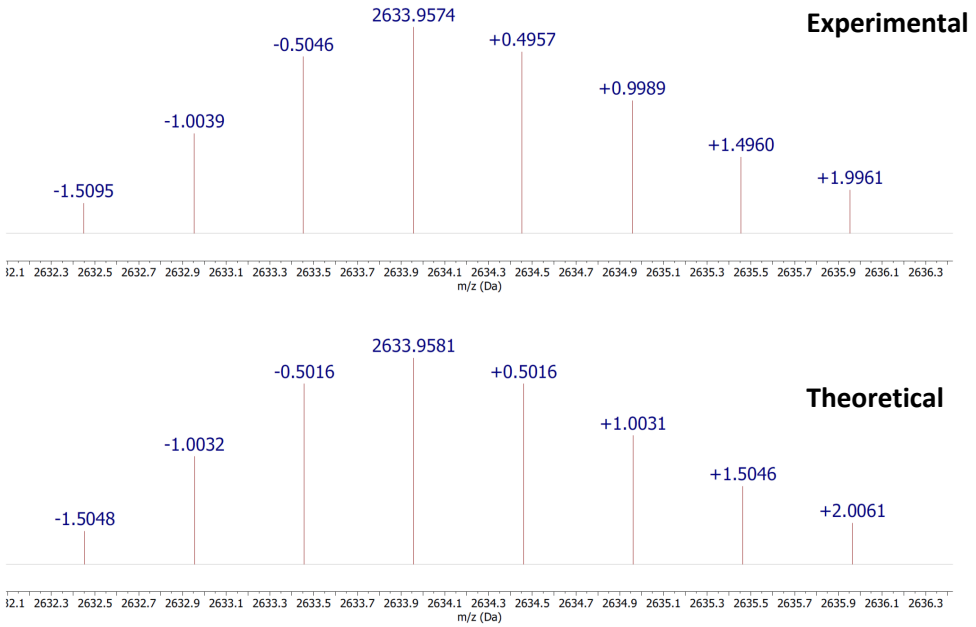

Figure S2c-4. Isotope distributions of ion $(\mathbf{H8})_2 \cdot \mathbf{OV}^{2+}$ in the 1:2 mixture of **H8** and $\mathbf{OV}^{2+} \bullet (\mathbf{PF_6}^-)_2$ (upper: from ESI-QTOF spectrum; bottom: from computer simulation). The mass difference between isotope peaks is about 0.5 (1/2).

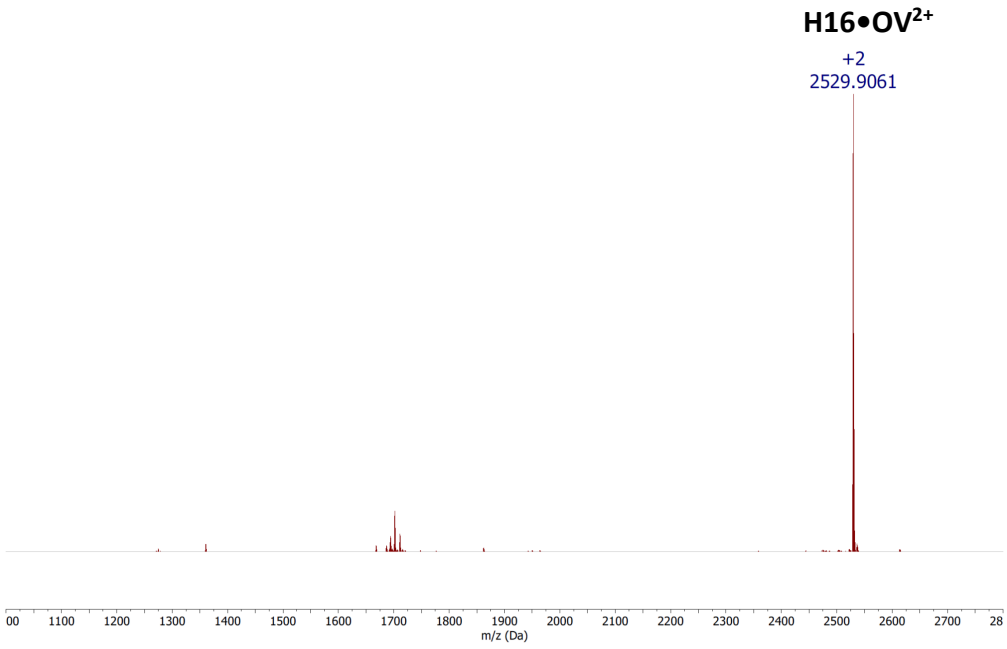

Figure S3a-1. High resolution electrospray-ionization quadrupole time-of-flight (ESI-TOF) spectra of the 1:1 mixture of **H16** and $\mathbf{OV}^{2+} \bullet (\mathbf{PF_6}^-)_2$.

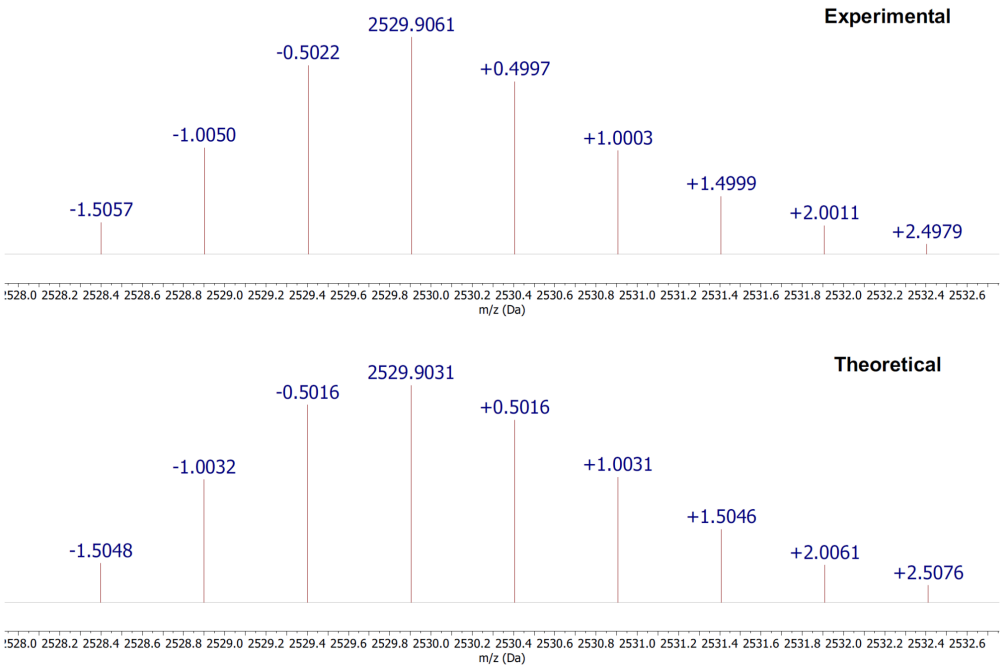

Figure S3a-2. Isotope distributions of ion **H16·OV^{2+}** in the 1:1 mixture of **H16** and **OV^{2+}•(PF$_6^-$)$_2$** (upper: from ESI-QTOF spectrum; bottom: from computer simulation). The mass difference between isotope peaks is about 0.5 (1/2).

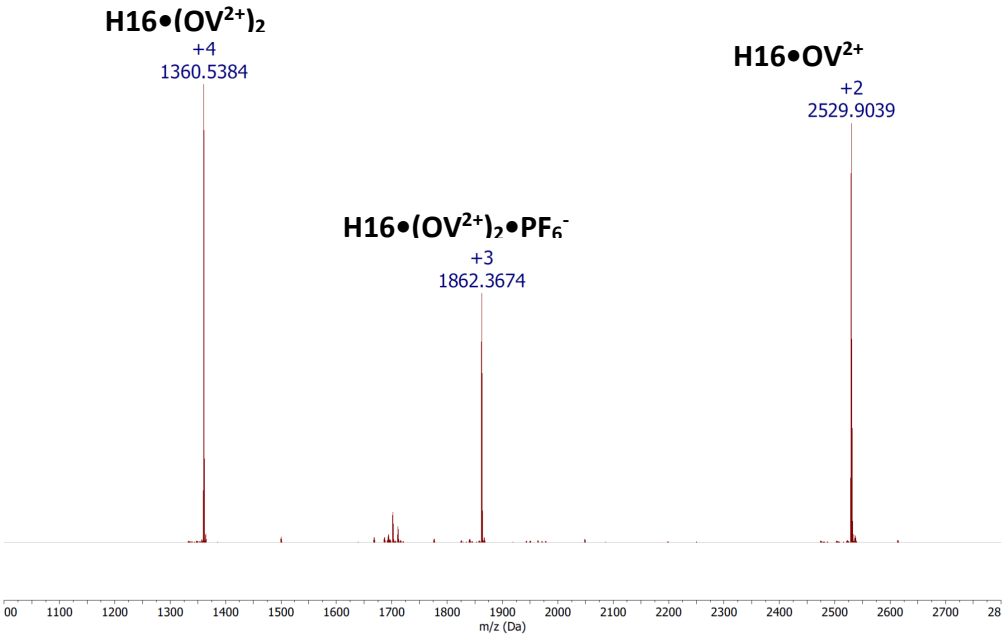

Figure S3b-1. High resolution electrospray-ionization quadrupole time-of-flight (ESI-TOF) spectra of the 1:2 mixture of **H16** and **OV^{2+}•(PF$_6^-$)$_2$.**

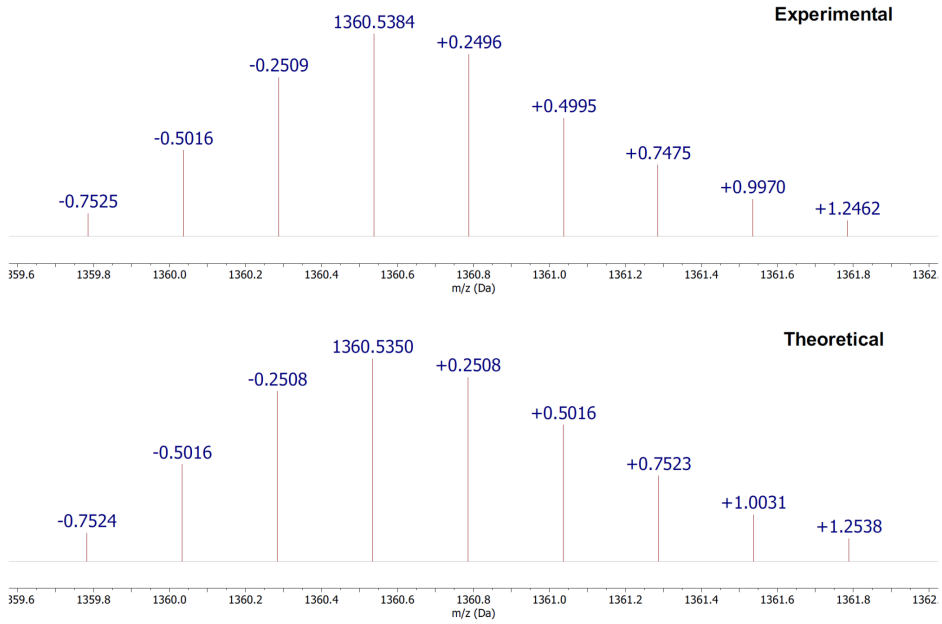

Figure S3b-2. Isotope distributions of ion **H16·(OV^{2+})$_2$** in the 1:2 mixture of **H16** and **OV^{2+}•(PF$_6^-$)$_2$** (upper: from ESI-QTOF spectrum; bottom: from computer simulation). The mass difference between isotope peaks is about 0.25 (1/4).

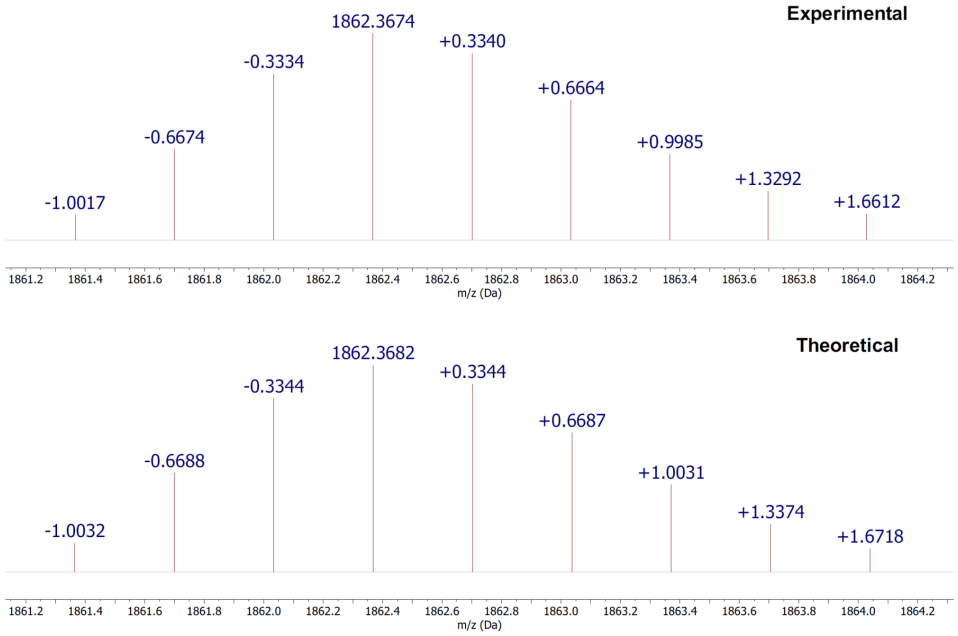

Figure S3b-3. Isotope distributions of ion **H16·(OV^{2+})$_2$•PF$_6^-$** in the 1:2 mixture of **H16** and **OV^{2+}•(PF$_6^-$)$_2$** (upper: from ESI-QTOF spectrum; bottom: from computer simulation). The mass difference between isotope peaks is about 0.33 (1/3).

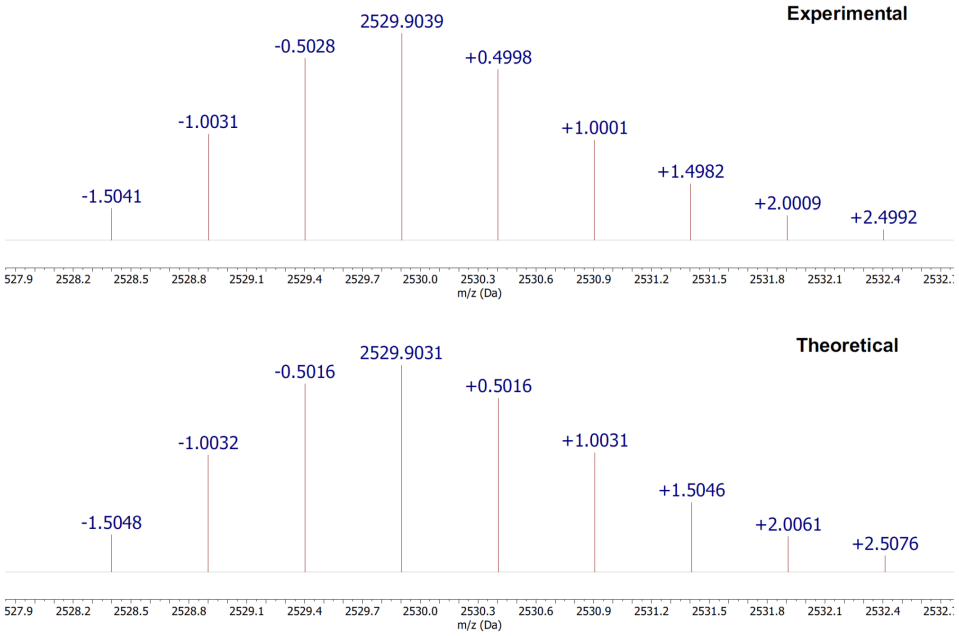

Figure S3b-4. Isotope distributions of ion **H16·OV^{2+}** in the 1:2 mixture of **H16** and **OV^{2+}•(PF_6^-)$_2$** (upper: from ESI-QTOF spectrum; bottom: from computer simulation). The mass difference between isotope peaks is about 0.5 (1/2).

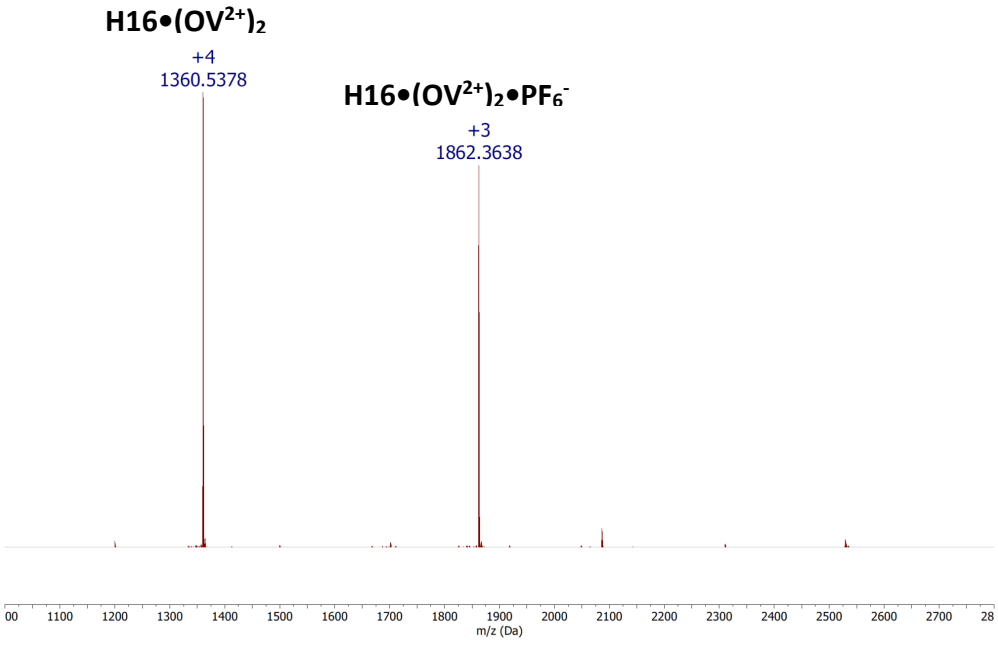

Figure S3c-1. High resolution electrospray-ionization quadrupole time-of-flight (ESI-TOF) spectra of the 1:4 mixture of **H16** and **OV^{2+}•(PF_6^-)$_2$.**

Figure S3c-2. Isotope distributions of ion **H16·(OV^{2+})$_2$** in the 1:4 mixture of **H16** and **OV^{2+}•(PF$_6^-$)$_2$** (upper: from ESI-QTOF spectrum; bottom: from computer simulation). The mass difference between isotope peaks is about 0.25 (1/4).

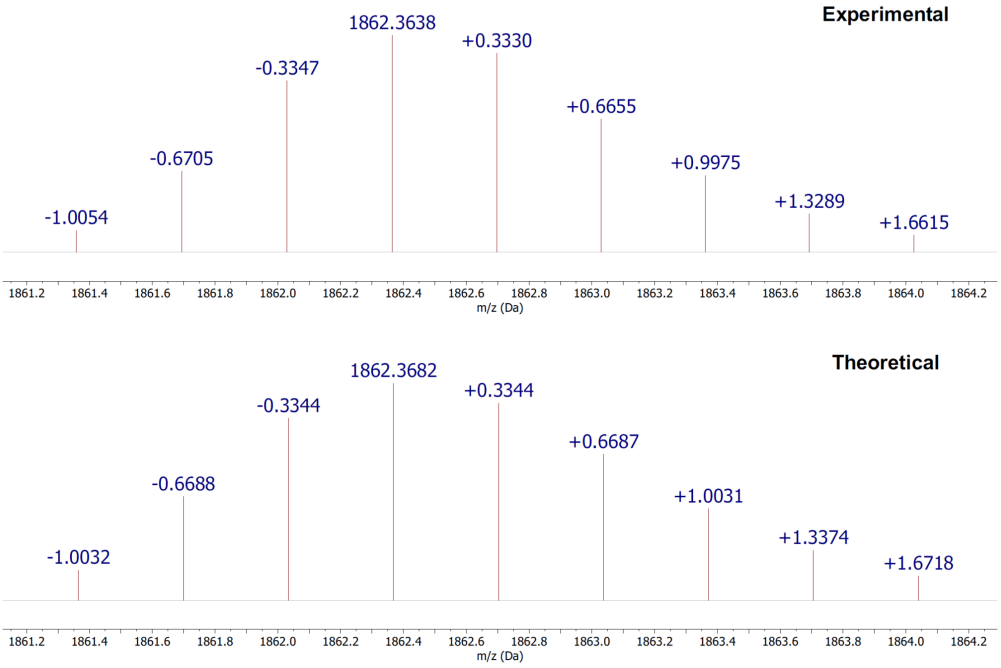

Figure S3c-3. Isotope distributions of ion **H16·(OV^{2+})$_2$•PF$_6^-$** in the 1:4 mixture of **H16** and **OV^{2+}•(PF$_6^-$)$_2$** (upper: from ESI-QTOF spectrum; bottom: from computer simulation). The mass difference between isotope peaks is about 0.33 (1/3).

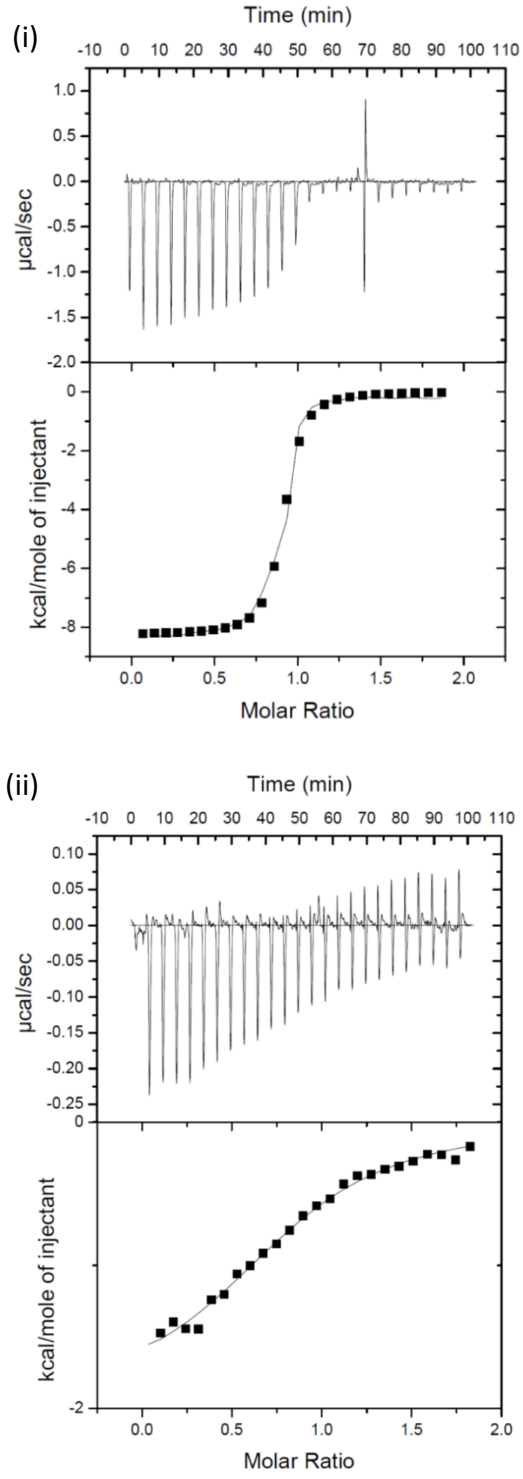

Figure S4a. (i) ITC titration curves (upper panel) and binding isotherms (lower panel) for the complexation of **H8** (50 µM) with **OV^{2+}•(PF_6^-)$_2$** (500 µM) in MeOH/$CHCl_3$ (3/7, v/v) at 35 °C. (ii) ITC titration curves (upper panel) and binding isotherms (lower panel) for the complexation of **H8** (50 µM) with **OV^{2+}•(PF_6^-)$_2$.** (500 µM) in DMSO/$CHCl_3$ (1/1, v/v) at 45 °C.

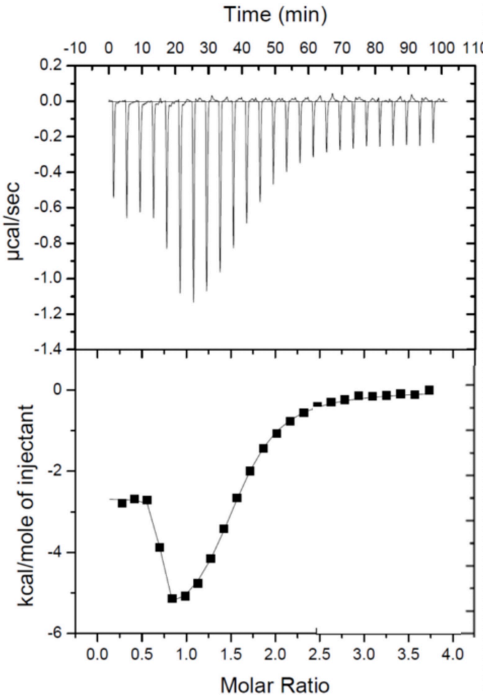

Figure S4b. ITC titration curves (upper panel) and binding isotherms (lower panel) for the titration of **H16** (25 µM) with $\mathbf{OV^{2+}\bullet(PF_6^-)_2}$ (500 µM) in MeOH/$CHCl_3$ (3/7, v/v) at 35 °C.

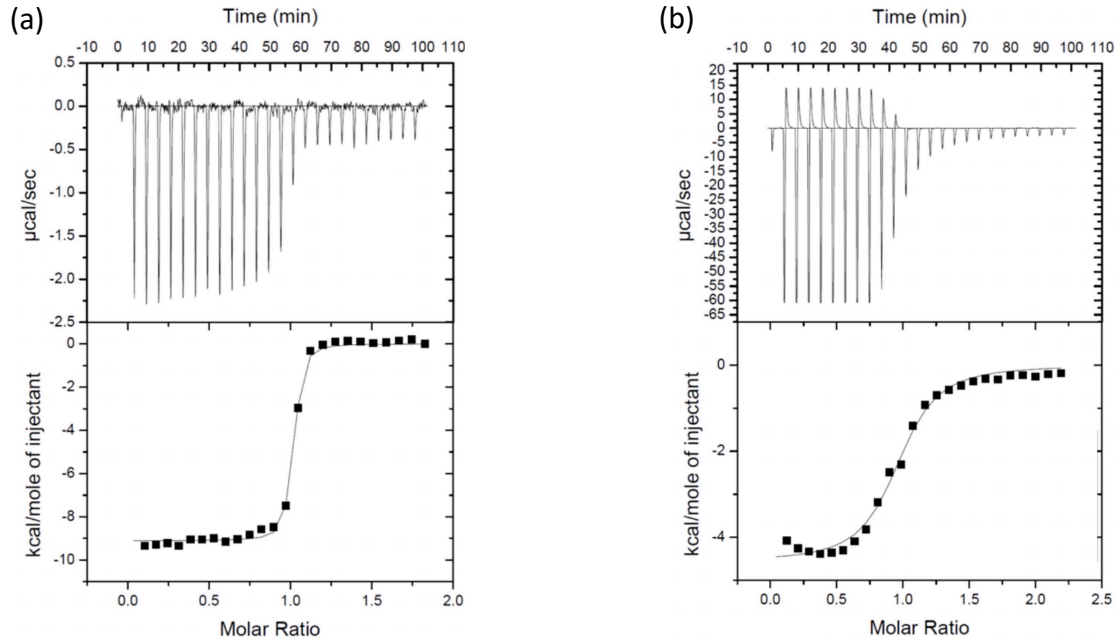

Figure S5. ITC titration curves (upper panel) and binding isotherms (lower panel) for the titration of (a) **H16** (50 µM) with $\mathbf{OV^{2+}\bullet(PF_6^-)_2}$ (500 µM) in DMSO/$CHCl_3$ (1/1, v/v) at 45 °C; and (b) **H16** (3 mM) and $\mathbf{OV^{2+}\bullet PF_6^-}$ (3 mM) with $\mathbf{OV^{2+}\bullet(PF_6^-)_2}$ (30 mM) in DMSO/$CHCl_3$ (1/1, v/v) at 45 °C.

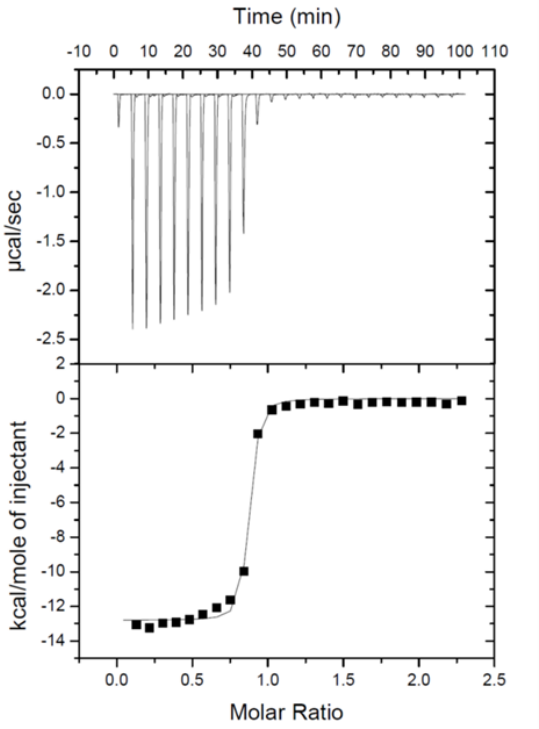

Figure S6. ITC titration curves (upper panel) and binding isotherms (lower panel) for the titration of **H16** (50 µM) with $\mathbf{TB^{2+}\bullet(PF_6^-)_2}$ (500 µM) in DMSO/$CHCl_3$ (1/1, v/v) at 45 °C.

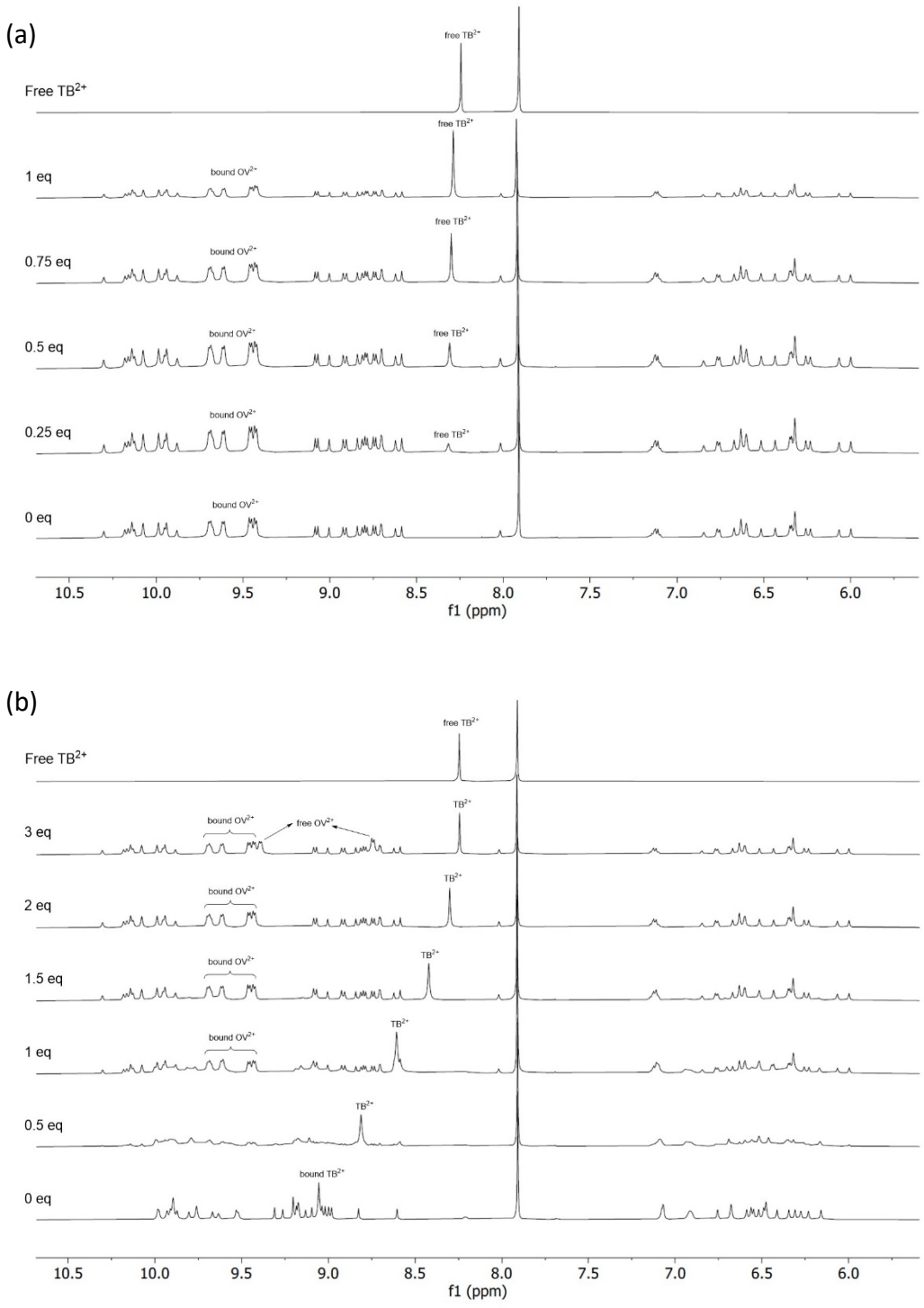

Figure S7. Partial ^{1}H NMR (500 MHz) of (a) **H16** (1 mM) and $\mathbf{OV^{2+}(PF_6^-)_2}$ (2 mM) titrated with $\mathbf{TB^{2+}(PF_6^-)_2}$ and, (b) **H16** (1 mM) with $\mathbf{TB^{2+}(PF_6^-)_2}$ (1 mM) titrated with $\mathbf{OV^{2+}(PF_6^-)_2}$ (in DMSO-d_6/$CDCl_3$ (2/3, v/v) at 45 ^{o}C).

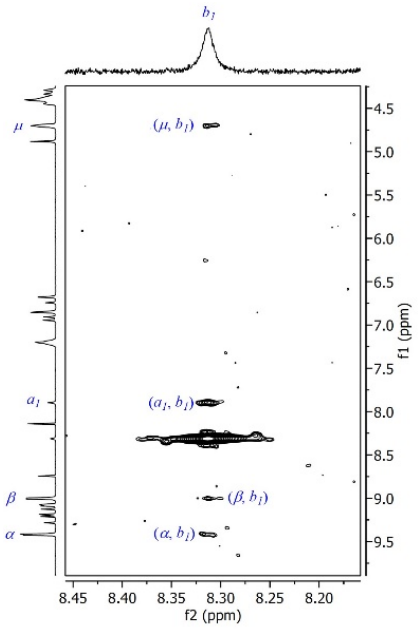

Figure S8. Partial NOESY (500 MHz, mix time: 500 ms) of **H8** (5 mM) and **OV^{2+}•$(PF_6^-)_2$** (5 mM) in DMSOd_6/$CDCl_3$ (7/3, v/v) at 45 °C.

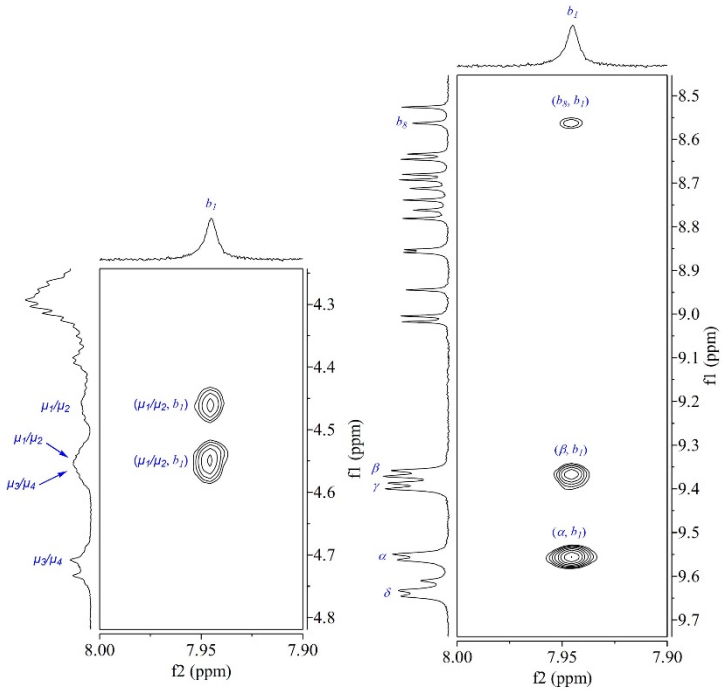

Figure S9. Partial NOESY (500 MHz, mix time: 500 ms) of **H16** (3 mM) and **OV^{2+}•$(PF_6^-)_2$** (6 mM) in DMSOd_6/$CDCl_3$ (2/3, v/v) at 45 °C.

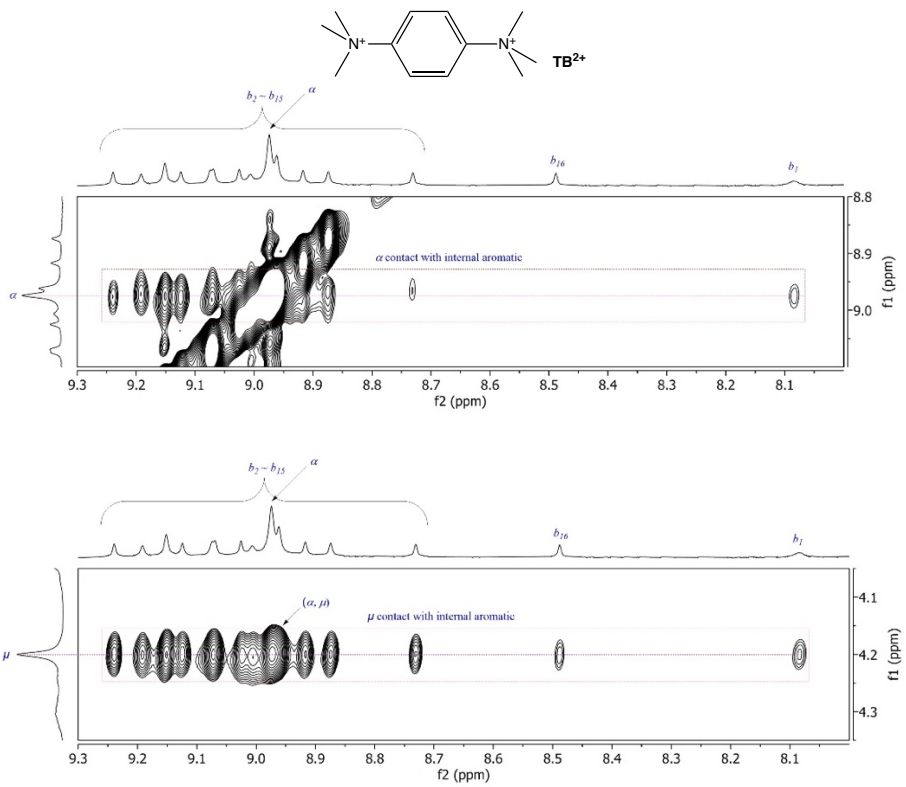

Figure S10. Partial NOESY (500 MHz, mix time: 500 ms) of **H16** (3 mM) and **TB^{2+}•$(PF_6^-)_2$** (3 mM) in DMSOd_6/$CDCl_3$ (1/1, v/v) at 45 °C.

II. General Information

Chemicals were purchased from commercial sources and used as received. Unless otherwise specified, all solvents were removed with a rotary evaporator. Silica gel for analytical thin layer chromatography (TLC) and column chromatography (mesh 230~400) were purchased from Sorbent Technologies Inc. 1H NMR spectra were recorded at 500 MHz at ambient temperature using $CDCl_3$ or DMSO-d6 as solvent (Cambridge Isotope Laboratories, Inc.) on Varian Inova-500. Chemical shifts are reported in parts per million (ppm) downfield from TMS (tetramethylsilane). High-resolution mass spectra were recorded on an Agilent 6530 Q-TOF LC/MS.

Synthetic procedure. The synthesis of **OV^{2+}**,[1] **H8**[2] and **H16**[2] was reported before. **TB^{2+}** was synthesized according to previously reported procedures.[3]

Isothermal Titration Calorimetry (ITC). The host (**H8** or **H16**) was placed in the cell and titrated with the guest (**$OV^{2+}\bullet(PF_6^-)_2$** or **$TB^{2+}\bullet(PF_6^-)_2$**) as the ligand. ITC experiments were performed using a MicroCal VP-ITC. In a typical ITC experiment, the reference cell was loaded with ~2 mL of solvent, the sample cell was loaded with ~1.5 mL of the host (**H8** or **H16**) at a concentration of 25 – 50 μM and the syringe was loaded with ~300 μL of guest (**$OV^{2+}\bullet(PF_6^-)_2$** or **$TB^{2+}\bullet(PF_6^-)_2$**) at a concentration of ~500 μM. During the experiment, 7.5 – 10 μL aliquots from the syringe were added to the sample cell for a total of 25 – 35 injections. Heats of dilution were obtained by titrating guest (**$OV^{2+}\bullet(PF_6^-)_2$** or **$TB^{2+}\bullet(PF_6^-)_2$**) into the ITC sample cell in the absence of host. These heats were found to be negligible when compared to the binding interaction heats. The resulting raw binding isotherm was then integrated, and the heats of injection were obtained. After importing the obtained data into the Origin software with MicroCal ITC add-on,[4] one site binding model is used for the fitting of the titration curve of **H8** with **$OV^{2+}\bullet(PF_6^-)_2$** in MeOH/$CHCl_3$ (3/7, v/v) at 35 ^oC or DMSO/$CHCl_3$ (1/1, v/v) at 45 ^oC, **H16** with **$TB^{2+}\bullet(PF_6^-)_2$** in DMSO/$CHCl_3$ (1/1, v/v) at 45 ^oC and each step(first binding event and second binding event) of **H16** with **$OV^{2+}\bullet(PF_6^-)_2$** in DMSO/$CHCl_3$ (1/1, v/v) at 45 ^oC. Sequential binding model is used for the fitting of the titration curve of **H16** with **$OV^{2+}\bullet(PF_6^-)_2$** in MeOH/$CHCl_3$ (3/7, v/v) at 35 ^oC.

III. Methods for X-ray Crystallography

Methods for crystallogenesis. Single crystals of the host-guest complexes were obtained via the liquid-liquid diffusion in an NMR tube of methanol in a dichloromethane solution of the host-guest complex (10 mg/mL).

Methods for solving the structures. single crystal X-ray diffraction data for host-guest complex structures were collected with a RigakuFRX rotating anode (2.97 kW) diffractometer at the IECB X-ray facility (CNRS UMS 3033 – INSERM US001, Université de Bordeaux). CuKα radiation monochromated with high flux Osmic Varimax mirrors was used for data collection. The X-ray source is equipped with an Eiger1M detector and an AFC11 partial chi goniometer allowing omega scans. The crystals were mounted on cryoloops and flashfrozen under a nitrogen gas stream at 130(2) K. Data were processed with the CrysAlisPRO software.[5] The structure were solved with the ShelXT[6] structure solution program using Intrinsic Phasing. The Olex2 suite[7] was used for models building and structures refinement with the ShelXL[8] package running Least Squares minimization. Only non-H atoms of the backbones, guests and side chains observable in the electron density maps were refined with anisotropic displacement parameters. For backbones and observable guests or side chains H atoms were positioned geometrically and constrained depending on their environment. Those H-atoms were refined in the riding-model approximation, with Uiso(H)=1.2Ueq (CH, CH2, NH). DFIX, AFIX, and SIMU restraints were apply to model geometry of the molecules and thermal motion parameters.

Refinement of large crystal structures faces problems usually observed in macromolecular crystallography, *i.e.* large volume fractions of disordered solvent molecules radiation damage and high thermal motion for long side chains leading to weak diffraction intensities, incompleteness of the data, moderate or low resolution. Thus, it is not surprising that a number of A-level and B-level alerts were detected using IUCR's checkcif algorithm. These alerts are inherent to the data and refinement procedures and do not reflect errors.

Table S1. Crystal data and structure refinement for **H16•$(VO^{2+})_2$**

Identification code	H16•$(VO^{2+})_2$
Empirical formula	$C_{448}H_{312}F_{42}N_{40}O_{126}P_7$
Formula weight	9286.15
Temperature/K	130(2)
Crystal system	monoclinic
Space group	C2/c
a/Å	41.464(2)
b/Å	37.476(2)
c/Å	43.380(2)
α/°	90
ß/°	99.771(5)
γ/°	90
Volume/Å^3	66430(6)
Z	4
ρ_{calc}g/cm^3	0.928
μ/mm^{-1}	0.806
F(000)	19084.0
Crystal size/mm^3	0.1 × 0.01 × 0.01
Radiation	CuKα (λ = 1.54178)
2Θ range for data collection/°	3.604 to 89.204
Reflections collected	130917
Independent reflections	25468 [R_{int} = 0.0766, R_{sigma} = 0.0676]
Data/restraints/parameters	25468/11840/2894
Goodness-of-fit on F^2	1.810
Final R indexes [I>=2σ (I)]	R_1 = 0.2210, wR_2 = 0.5107
Final R indexes [all data]	R_1 = 0.2999, wR_2 = 0.5612

Table S2. Crystal data and structure refinement for **$(H8)_2$•$(VO^{2+})_2$**

Identification code	$(H8)_2$•$(VO^{2+})_2$
Empirical formula	$C_{599}H_{792}F_{48}N_{40}O_{139}P_8$
Formula weight	11936.44
Temperature/K	130(2)
Crystal system	monoclinic
Space group	$P2_1/n$
a/Å	27.6163(5)
b/Å	45.0146(5)
c/Å	28.5060(4)
α/°	90
β/°	112.072(2)
γ/°	90
Volume/Å^3	32839.8(9)
Z	2
ρ_{calc}g/cm^3	1.207
μ/mm^{-1}	0.965
F(000)	12660.0
Crystal size/mm^3	0.1 × 0.1 × 0.1
Radiation	CuKα (λ = 1.54178)
2Θ range for data collection/°	6.572 to 123.584
Reflections collected	146992
Independent reflections	50210 [R_{int} = 0.0283, R_{sigma} = 0.0338]
Data/restraints/parameters	50210/3182/3920
Goodness-of-fit on F^2	1.726
Final R indexes [I>=2σ (I)]	R_1 = 0.1342, wR_2 = 0.4000
Final R indexes [all data]	R_1 = 0.1605, wR_2 = 0.4258

IV. References

1. T. A. Sobiech, Y. Zhong, J. K. McGrath, C. Scalzo, E. Zurek, B. Gong, B. L. S. Sanchez, D. P. Miller, B. Kauffmann, Y. Ferrand and I. Huc, *Chem. Commun.*, 2021, **57**, 11645–11648.
2. Y. Zhong, B. Kauffmann, W. Xu, Z.-L. Lu, Y. Ferrand, I. Huc, X. C. Zeng, R. Liu and B. Gong, *Org. Lett.*, 2020, **22**, 6938-6942.
3. *CN*. *Pat*., CN108545978, 2018.
4. ITC Data Analysis in Origin®: Tutorial Guide Version 7.0, MicroCal, Northhampton MA, 2004, 108-109.
5. Rigaku Oxford Diffraction (2015). CrysAlis PRO. RigakuOxford Diffraction, Yarnton, England.
6. G. M. Sheldrick, *Acta Cryst*., 2015, **A71**, 3-8.
7. O. V. Dolomanov, L. J. Bourhis, R. J. Gildea, J. A. K. Howard and H. Puschmann, *J. Appl. Cryst*., 2009, **42**, 339-341.
8. G. M. Sheldrick, *Acta Cryst*., 2015, **C71**, 3-8.